REPORT DOCUMENTATION PAGE

Form Approved
OMB NO. 0704-0188

Public Reporting burden for this collection of information is estimated to average 1 hour per response, including the time for reviewing instructions, searching existing data sources, gathering and maintaining the data needed, and completing and reviewing the collection of information. Send comment regarding this burden estimates or any other aspect of this collection of information, including suggestions for reducing this burden, to Washington Headquarters Services, Directorate for information Operations and Reports, 1215 Jefferson Davis Highway, Suite 1204, Arlington, VA 22202-4302, and to the Office of Management and Budget, Paperwork Reduction Project (0704-0188,) Washington, DC 20503.

1. AGENCY USE ONLY (Leave Blank)

2. REPORT DATE
11/15/00

3. REPORT TYPE AND DATES COVERED
Final Report (8/98 - 2/99)

4. TITLE AND SUBTITLE
High-Order Sparse Matrix Nyström Algorithm for the Analysis of Planar Microwave Circuits

5. FUNDING NUMBERS
DAAG55-98-1-0460

6. AUTHOR(S)
Stephen D. Gedney

7. PERFORMING ORGANIZATION NAME(S) AND ADDRESS(ES)
University of Kentucky
Dept. of Electrical Engineering
453 Anderson Hall, Lexington, KY 40506-0046

8. PERFORMING ORGANIZATION REPORT NUMBER

9. SPONSORING / MONITORING AGENCY NAME(S) AND ADDRESS(ES)
U. S. Army Research Office
P.O. Box 12211
Research Triangle Park, NC 27709-2211

10. SPONSORING / MONITORING AGENCY REPORT NUMBER
ARO 39075.1-EL-11

11. SUPPLEMENTARY NOTES
The views, opinions and/or findings contained in this report are those of the author(s) and should not be construed as an official Department of the Army position, policy or decision, unless so designated by other documentation.

12 a. DISTRIBUTION / AVAILABILITY STATEMENT
Approved for public release; distribution unlimited.

12 b. DISTRIBUTION CODE

13. ABSTRACT (Maximum 200 words)

The focus of this research has been on the development of a fast high-order solution method for the analysis of large scale printed microwave circuit devices. The method is based on a high-order sparse matrix/Nyström (SM/N) method. The goal is to develop a scheme that provides controllable accuracy, fast error convergence, and fast solutions for the simulation of large practical circuits. This intent of the 6 month STIR was to initiate this research and demonstrate a proof of concept. To this end, in this program we have developed a locally corrected Nyström scheme that exhibits true high-order convergence for electromagnetic scattering simulations. This is demonstrated for both smooth objects, as well as objects with edge singularities. Secondly, in pursuant of a high-order scheme for the simulation of circuits printed in layered media, a fast computation of the Sommerfeld Green's functions to controllable accuracy has been developed.

14. SUBJECT TERMS
locally corrected Nyström method, microwave circuit design, high-order technique

15. NUMBER OF PAGES
41

16. PRICE CODE

17. SECURITY CLASSIFICATION OR REPORT
UNCLASSIFIED

18. SECURITY CLASSIFICATION ON THIS PAGE
UNCLASSIFIED

19. SECURITY CLASSIFICATION OF ABSTRACT
UNCLASSIFIED

20. LIMITATION OF ABSTRACT
UL

NSN 7540-01-280-5500

Standard Form 298 (Rev.2-89)
Prescribed by ANSI Std. 239-18
298-102

20010116 124

DTIC QUALITY INSPECTED 3

CONTENTS

1. INTRODUCTION **2**

2. THE LOCALLY CORRECTED NYSTRÖM METHOD **4**

3. APPLICATION OF THE LCN METHOD TO THE EFIE **6**

- 3.1 THE NYSTRÖM FORMULATION OF THE EFIE 6
- 3.2 LOCALLY CORRECTING G^R 11
  - *3.2.1 Patch Based Local Corrections* *11*
  - *3.2.2 Evaluating the Self Patch* *13*

4. APPLICATION OF THE LCN METHOD TO THE MFIE **16**

- 4.1 THE MFIE 16
- 4.2 THE LOCALLY CORRECTED NYSTRÖM FORMULATION OF THE MFIE 19

5. NUMERICAL VALIDATION OF THE NYSTRÖM SOLUTION **21**

6. MULTILAYERED GREEN'S FUNCTION COMPUTATION **28**

- 6.1 THE MPIE 28
- 6.2 EFFICIENT COMPUTATION OF THE SOMMERFELD INTEGRAL 29
- 6.3 INTERPOLATION OF THE GREEN'S FUNCTION 35

7. CONCLUSIONS **38**

REFERENCES **39**

1. Introduction

When computing the electromagnetic interaction with large complex geometries there is generally a trade off between the solution accuracy and the degrees-of freedom representing the discrete surface current densities. Most popular electromagnetic scattering codes based on method of moment (MoM) solutions employ low-order basis functions and testing functions. That is functions that lead to fixed error convergence rates that are typically $O(h^2)$ or less. Unfortunately, such techniques are deficient in that:

- Typical simulations employing 10 to 20 unknowns per linear wavelength provide 3 - 5 % accuracy.
- If increased accuracy is required from the simulation, a significant increase in the computational resources is necessary as characterized by low-order convergence. In fact, codes employing the popular Rao-Wilton-Gliss (RWG) basis [1] realize only linear convergence. That is, a factor of two increase in the number of unknowns only reduces the error by a factor of two.
- Efficient predictions of solution error is not possible.

In contrast to a low-order scheme, a high-order method is defined as being not just a scheme that can provide high orders of convergence, but also a scheme that allows one to control the *rate* of convergence. That is, for a fixed order p, one can decrease the mesh size h realizing a geometric rate of convergence $O(h^p)$. Or, one can increase the order p to realize an exponential rate of convergence. Furthermore, a high-order technique should be capable of substantially reducing the solution error at the expense of only a modest increase in computational resources and complexity.

The locally corrected Nyström (LCN) method has demonstrated high-order error convergence for RCS computations [2, 3] and has been shown to be computationally efficient. The LCN method has the distinct advantages that:

- The error convergence can be increased exponentially by simply increasing the quadrature order of the underlying Nyström scheme, avoiding remeshing for higher accuracies.
- By controlling error convergence, mathematical error estimates can be obtained efficiently.
- The computation of matrix elements is computationally efficient. Typically, this is dominated by constructing a sparse local correction matrix, which is $O(N)$).
- Improving solution error typically requires one to simply increase the quadrature order on the patches - thus avoiding remeshing.
- Curvilinear meshing allows for cells that can have linear dimensions that are in excess of a wavelength on a side. This is amenable to wide band simulations that allow for a coarse meshing that can be applicable to a very broad spectrum of frequencies. Accuracy is then controlled by simply manipulating the number of quadrature points.
- The point based discretization is amenable to fast methods

High-order MoM solutions are also realizable by employing higher-order basis and testing functions [4, 5]. However, experience has shown that the LCN technique is more efficient and of lower complexity than the MoM. The fill time for the MoM solution is $O(N^2)$ and is burdened by the double numerical integrations required to compute the entries of the impedance matrix to sufficient accuracy. This is in contrast to the single integrations required for the local corrections of the LCN method. Furthermore, when exploiting large patches (possibly one or two wavelengths along linear dimension), the point-based discretization of the LCN simplifies the grouping required by fast methods.

The focus of this paper is to provide an in depth development of the locally-corrected Nyström scheme as applied to the electric field and magnetic field integral equations. Section 2 outlines the general locally corrected Nyström scheme. Section 3 provides an in depth treatment of performing the exact integrations of the kernel convolved with the basis functions for the electric field integral equation. Section 4 then treats the magnetic field integral equation. Section 5 then details the computational treatment of the local corrections for general basis. Finally, Section 6 provides some numerical validation.

2. The Locally Corrected Nyström Method

The Nyström method [2, 6] is a simple technique that provides an efficient high-order solution of integral equations. Consider the integral equation:

$$\phi(\vec{r}) = \int_{\Omega} G(\vec{r} - \vec{r}\,')J(\vec{r}\,')ds' \tag{2.1}$$

where $J(\vec{r}\,')$ is an unknown current density, $\phi(\vec{r})$ is the known forcing function evaluated at position $\vec{r}$, and G is a non-singular kernel. It is assumed that a numerical quadrature rule can be defined over the domain Ω that can compute the convolutional integral to a desired accuracy. Defining the abscissas and weights of a N-th order quadrature rule to be $(\vec{r}\,'_n, \omega_n)$, (2.1) is approximated as:

$$\phi(\vec{r}) \approx \sum_{n=1}^{N} \omega_n G(\vec{r} - \vec{r}\,'_n)J(\vec{r}\,'_n). \tag{2.2}$$

Then, sampling (2.2) at the N abscissa points leads to a square linear system of equations with the m-th equation expressed as:

$$\phi(\vec{r}_m) = \sum_{n=1}^{N} \omega_n G(\vec{r}_m - \vec{r}\,'_n)J(\vec{r}\,'_n) \tag{2.3}$$

This provides for a solution for $J(\vec{r})$ at the discrete points $\vec{r}\,'_n$. Assuming that the geometry is smooth and G is non-singular, the order of the accuracy would be commensurate with the underlying quadrature rule. Thus, if the quadrature rule is exponentially convergent, the solution for the unknown current will be as well.

Unfortunately, the Nyström method cannot be applied directly to singular kernels. This is true for the obvious reasons: 1) numerical quadrature integrates singular functions to low order, and 2) if $G(\vec{r}_m - \vec{r}\,'_n)$ is infinite when $\vec{r}_m = \vec{r}\,'_n$, then (2.3) is ill posed. To circumvent this, a modified technique known as the locally corrected Nyström (LCN) method [2, 6] has been introduced. To this end, let

$$G_{m,n} = \begin{cases} G(\vec{r}_m - \vec{r}\,'_n), & m \neq n \\ 0, & m = n \end{cases} \tag{2.4}$$

be the *discrete kernel* represented in (2.3). Next, define an *exact kernel* to be $\bar{G}_{m,n}$. Then, a *local correction matrix* $L_{m,n}$ is introduced such that

$$\bar{G}_{m,n} = G_{m,n} + L_{m,n}. \tag{2.5}$$

That is, the superposition of the local correction matrix with the discrete kernel renders the exact kernel.

The idea of the local corrections is to introduce a new quadrature rule that is specialized to the convolutional integral and that is exact for a specific class of functions. Assume that the current density J is expanded into a set of known basis functions $f_k(\vec{r})$ that are distributed over Ω. Then, from (2.5), define the operator:

$$\sum_{n=1}^{N} \omega_n L_{m,n} f_k(\vec{r}_n) = \int_{\Omega} G(\vec{r}_m - \vec{r}') f_k(\mathbf{r}')\, ds' - \sum_{\substack{n=1 \\ n \neq m}}^{N} \omega_n G_{m,n} f_k(\vec{r}_n) \tag{2.6}$$

Expressing this for K basis functions $f_k(\vec{r})$ leads to a linear system of equations on the left-hand-side of (2.6), which is used to solve for the the m-th row of the local correction, $L_{m,n}$. The right-hand-side of (2.6) corresponds to the residual error of the discrete approximation of the convolution relative to the exact convolution of the kernel with $f_k(\vec{r})$. The linear system of equations is solved using a direct LU factorization if $K = N$ or singular value decomposition if $K \neq N$.

For problems that are sufficiently large, $L_{m,n}$ is a sparse matrix. This arises since away from the singularity $G(\vec{r}_m - \vec{r}'_n)$ becomes a smooth function. Subsequently, in this region numerical quadrature approximates (2.1) to high-order. Thus, as $|\vec{r}_m - \vec{r}'_n|$ becomes sufficiently large, the residual error on the right-hand-side of (2.6) tends to zero and entries of $L_{m,n}$ become negligibly small.

Once $L_{m,n}$ is constructed, (2.3)-(2.5) are combined, leading to the linear system of equations:

$$\phi(\vec{r}_m) = \sum_{n=1}^{N} \omega_n \left(G_{m,n} + L_{m,n}\right) J(\vec{r}'_n) \tag{2.7}$$

which is used to solve for the unknown current density vector.

The Nyström method has the distinct advantages that:

- The discrete kernel $G_{m,n}$ is computed simply from one point evaluations of the kernel.
- The local correction matrix is sparse, and only needs to be computed in the near vicinity of the observation point. Thus, constructing $L_{m,n}$ requires $O(N)$ operations.
- Increasing the convergence order simply requires an increase in the number of quadrature points.
- The method provides a smooth approximation for the currents over the surface Ω that is represented by an expansion of the functional basis of the underlying quadrature rule.

3. Application of the LCN Method to the EFIE

3.1 The Nyström Formulation of the EFIE

Consider the electromagnetic scattering by a three-dimensional PEC object situated in a free space. The relationship between the equivalent currents on the surface of the object and the scattered electric field can be expressed as:

$$\vec{E}^s = -jk_o\eta_o \int_S \vec{J}(\vec{r}')G(\vec{r},\vec{r}')ds' - j\frac{\eta_o}{k_o}\nabla\int_S \left(\nabla G(\vec{r},\vec{r}')\cdot\vec{J}(\vec{r}')\right)ds' \tag{3.1}$$

where $G(\vec{r},\vec{r}')$ is the free-space Green's function:

$$G(\vec{r},\vec{r}\,') = \frac{e^{-jk|\vec{r}-\vec{r}\,'|}}{4\pi|\vec{r}-\vec{r}\,'|}. \tag{3.2}$$

Initially, it is assumed that the surface S is discretized using curvilinear patches that represents the surface curvature to high-order. It is assumed that the surface of the patch can be uniquely described by a two-dimensional curvilinear space $\left(u^1,u^2\right)$. The unitary vectors $\vec{a}_1$ and $\vec{a}_2$ defined for this space are described as [7]:

$$\vec{a}_i = \frac{\partial\vec{r}}{\partial u^i} \tag{3.3}$$

where $\vec{r} = \vec{r}(u^1,u^2)$. By definition, $\vec{a}_1$ and $\vec{a}_2$ are independent vectors that are tangential to the surface. Next, the coefficients of the metric tensor are defined as

$$g_{i,j} = \vec{a}_i \cdot \vec{a}_j. \tag{3.4}$$

The Jacobian is the square root of determinant of the metric tensor. Hence, the Jacobian for a surface integration is

$$\sqrt{g} = \sqrt{g_{1,1}g_{2,2} - g_{1,2}^2}. \tag{3.5}$$

The PEC body is assumed to be illuminated by an incident wave, defined by the electric field $\vec{E}^{inc}$. The resulting total tangential electric field must be zero on the PEC surface. Then, given $\vec{E}^{total} = \vec{E}^{inc} + \vec{E}^s$ and (3.1) the total tangential electric field is constrained to zero on the PEC surface, resulting in the electric field integral equation (EFIE):

$$-\vec{a}_i\cdot\vec{E}^{inc} = -jk_o\eta_o\int_S\left(\vec{a}_i\cdot\vec{J}(\vec{r}')\right)G(\vec{r},\vec{r}')ds' - j\frac{\eta_o}{k_o}\vec{a}_i\cdot\nabla\int_S\left(\nabla G(\vec{r},\vec{r}')\cdot\vec{J}(\vec{r}')\right)ds' \tag{3.6}$$

where $\vec{a}_i$ $(i=1,2)$ are the unitary vectors.

The focus of this section is the Nyström solution of (3.3) for the equivalent surface current density $\vec{J}(\vec{r}\,')$. Following the scheme presented in Section 2, first the underlying Nyström formulation must be derived as in (2.3). To this end, a numerical quadrature scheme is introduced over each curvilinear patch. Assuming that there are P patches, and N_{qp} quadrature points on the pth patch. Furthermore, the vector surface current density $\vec{J}(\vec{r}\,')$ is projected onto the two independent unitary vectors. Hence, it is approximated as:

$$\vec{J}(\vec{r}_n^{\,\prime}) = \frac{J_{1_n}\vec{a}_{1_n}^{\,\prime} + J_{2_n}\vec{a}_{2_n}^{\,\prime}}{\sqrt{g_n'}} \tag{3.7}$$

where J_{1_n} and J_{2_n} are constant coefficients affiliated with the abscissa point $\vec{r}_n^{\,\prime}$, $\vec{a}_{1_n}^{\,\prime}$ and $\vec{a}_{2_n}^{\,\prime}$ are the unitary vectors evaluated at $\vec{r}_n^{\,\prime}$, and $\sqrt{g_n'}$ is the Jacobian evaluated at $\vec{r}_n^{\,\prime}$. Finally, applying numerical quadrature to (3.6) and using (3.7) results in the discrete equation:

$$\begin{aligned} -\vec{a}_{i_m}\cdot\vec{E}^{inc}(\vec{r}_m) \approx & -jk_o\eta_o\sum_{p=1}^{P}\sum_{n=1}^{N_{qp}}\vec{a}_{i_m}\cdot\left(\frac{J_{1_n}\vec{a}_{1_n}^{\,\prime} + J_{2_n}\vec{a}_{2_n}^{\,\prime}}{\sqrt{g_n'}}\right)G(\vec{r}_m,\vec{r}_n^{\,\prime})\sqrt{g_n'}\,\omega_n \\ & - j\frac{\eta_o}{k_o}\sum_{p=1}^{P}\sum_{n=1}^{N_{qp}}\vec{a}_{i_m}\cdot\nabla\left(\nabla G(\vec{r}_m,\vec{r}_n^{\,\prime})\cdot\left(\frac{J_{1_n}\vec{a}_{1_n}^{\,\prime} + J_{2_n}\vec{a}_{2_n}^{\,\prime}}{\sqrt{g_n'}}\right)\right)\sqrt{g_n'}\,\omega_n \end{aligned} \tag{3.8}$$

where $(\vec{r}_n,\omega_n)$ are the abscissa and weight pair for the pth patch, and for $i = 1,2$.

The expression in (3.8) leads to the discrete kernel $G_{m,n}$, which can be expressed as a linear system of equations:

$$\begin{pmatrix} -\vec{a}_{1_m}\cdot\vec{E}^{inc}(\vec{r}_m) \\ -\vec{a}_{2m}\cdot\vec{E}^{inc}(\vec{r}_m) \end{pmatrix} = \begin{bmatrix} G_{m,n_{1,1}} & G_{m,n_{1,2}} \\ G_{m,n_{2,1}} & G_{m,n_{2,2}} \end{bmatrix}\begin{pmatrix} J_{1_n} \\ J_{2_n} \end{pmatrix} \tag{3.9}$$

In the second term of (3.8), there is a double gradient operation. Since the surface current density is expressed simply as a vector with unknown constant coefficients, the derivatives of the gradients must be restricted to operate on the free-space Green's function. This operation must then be derived to explicitly express the entries of the discrete kernel.

In order to understand more concretely specific terms of the discrete kernel, the free-space Green's function is expressed in terms of its real and imaginary parts. Specifically, (3.2) is written as:

$$G(\vec{r},\vec{r}\,') = G^R(\vec{r},\vec{r}\,') - jG^I(\vec{r},\vec{r}\,') = \frac{1}{4\pi}\left[\frac{\cos(k|\vec{r}-\vec{r}\,'|)}{|\vec{r}-\vec{r}\,'|} - j\frac{\sin(k|\vec{r}-\vec{r}\,'|)}{|\vec{r}-\vec{r}\,'|}\right]. \tag{3.10}$$

It is immediately seen that G^R is singular, whereas G^I is a regular function (i.e., G^I and all derivatives of G^I are bounded at vanishing separation of $\vec{r}$ and $\vec{r}\,'$).

Using this decomposition of the Green's function, the $\nabla\left(\nabla G(\vec{r},\vec{r}')\cdot\vec{J}(\vec{r}')\right)$ term can be evaluated separately for G^R and G^I. It can be shown that:

$$\begin{aligned}\vec{a}_i\cdot\nabla\left(\left(\nabla G^R(\vec{r},\vec{r}\,')\right)\cdot\vec{J}(\vec{r}\,')\right) &= -\vec{a}_i\cdot\vec{J}(\vec{r}\,')k^3\left[\frac{\sin kR}{(kR)^2}+\frac{\cos kR}{(kR)^3}\right]\\ &+\vec{a}_i\cdot(\vec{r}-\vec{r}\,')\vec{J}(\vec{r}\,')\cdot(\vec{r}-\vec{r}\,')k^5\left[3\frac{\cos kR}{(kR)^5}+3\frac{\sin kR}{(kR)^4}-\frac{\cos kR}{(kR)^3}\right],\end{aligned} \tag{3.11a}$$

$$\begin{aligned}\vec{a}_i\cdot\nabla\left(\left(\nabla G^I(\vec{r},\vec{r}\,')\right)\cdot\vec{J}(\vec{r}\,')\right) &= -\vec{a}_i\cdot\vec{J}(\vec{r}\,')k^3\left[\frac{\cos kR}{(kR)^2}-\frac{\sin kR}{(kR)^3}\right]\\ &+\left(\vec{a}_i\cdot(\vec{r}-\vec{r}\,')\right)\left(\vec{J}(\vec{r}\,')\cdot(\vec{r}-\vec{r}\,')\right)k^5\left[3\frac{\sin kR}{(kR)^5}-3\frac{\cos kR}{(kR)^4}-\frac{\sin kR}{(kR)^3}\right]\end{aligned} \tag{3.11b}$$

where $R=|\vec{r}-\vec{r}\,'|$. In deriving (3.11a) and (3.11b), the vector identity is used where:

$$\vec{a}_i\cdot\nabla\left(\frac{(\vec{r}-\vec{r}\,')}{R}\cdot\vec{J}(\vec{r}\,')\right)=\frac{\vec{a}_i\cdot\vec{J}(\vec{r}\,')}{R}-\frac{\left(\vec{a}_i\cdot(\vec{r}-\vec{r}\,')\right)\left(\vec{J}(\vec{r}\,')\cdot(\vec{r}-\vec{r}\,')\right)}{R^3} \tag{3.12}$$

The expressions from (3.10) and (3.11a,b) can then be used within (3.8). To this end, the discrete kernel in (3.9) is expressed as:

$$G_{m,n_{i,j}} = G^R_{m,n_{i,j}} + G^I_{m,n_{i,j}}\,. \tag{3.13}$$

where, $G^R_{m,n_{i,j}}$ arises from G^R, and $G^I_{m,n_{i,j}}$ from G^I. Subsequently,

$$\begin{aligned}G^R_{m,n_{i,j}} = -j\frac{\eta_o}{4\pi}\omega_n\Bigg[&k^2\left(\vec{a}_{i_m}\cdot\vec{a}'_{j_n}\right)\left[\frac{\cos kR_{m,n}}{kR_{m,n}}-\frac{\sin kR_{m,n}}{(kR_{m,n})^2}-\frac{\cos kR_{m,n}}{\left(kR_{m,n}\right)^3}\right]\\ &+k^4\left(\vec{a}_{i_m}\cdot\vec{R}_{m,n}\right)\left(\vec{a}'_{j_n}\cdot(\vec{r}_m-\vec{r}'_n)\right)\left[3\frac{\cos kR_{m,n}}{(kR_{m,n})^5}+3\frac{\sin kR_{m,n}}{(kR_{m,n})^4}-\frac{\cos kR_{m,n}}{(kR_{m,n})^3}\right]\Bigg]\end{aligned} \tag{3.14a}$$

$$G^I_{m,n_{i,j}} = \frac{\eta_o}{4\pi}\omega_n \left[k^2 \left(\vec{a}_{i_m} \cdot \vec{a}'_{j_n}\right) \left[-\frac{\sin kR_{m,n}}{kR_{m,n}} + \frac{\frac{\sin kR_{m,n}}{kR_{m,n}} - \cos kR_{m,n}}{\left(kR_{m,n}\right)^2} \right] + k^4 \left(\vec{a}_i \cdot \vec{R}_{m,n}\right)\left(\vec{a}'_{j_n} \cdot \vec{R}_{m,n}\right) \left[\frac{\frac{\sin kR_{m,n}}{kR_{m,n}} - 3\,\frac{\frac{\sin kR_{m,n}}{kR_{m,n}} - \cos kR_{m,n}}{\left(kR_{m,n}\right)^2}}{\left(kR_{m,n}\right)^2} \right] \right] \tag{3.14b}$$

where $\vec{R}_{m,n} = (\vec{r}_m - \vec{r}'_n)$ and $R_{m,n} = \left|\vec{R}_{m,n}\right|$.

The expression in (3.14a) is clearly hypersingular in the limit that $R_{m,n} \to 0$. Subsequently, this term must not only be locally corrected for a well-posed Nyström formulation - this term must also be specially treated such that the numerical integration required for the exact kernel is convergent. On the other hand, as expected, the integrand of (3.14b) is regular and hence is integrable to high-precision using a numerical quadrature. This is observed by performing a Taylor series expansion of the trigonometric terms and observing their value in the limit that R tends to zero:

$$\lim_{R\to 0}\left(\frac{\sin kR}{kR}\right) = 1 \tag{3.15a}$$

$$\lim_{R\to 0}\left(\frac{\frac{\sin kR}{kR} - \cos kR}{(kR)^2}\right) = \left(\frac{\frac{kR - \frac{(kR)^3}{3!} + \cdots}{kR} - (1 - \frac{(kR)^2}{2!} + \cdots)}{(kR)^2}\right) = \frac{1}{3} \tag{3.15b}$$

$$\lim_{R\to 0}\left(\frac{\dfrac{\sin kR}{kR}-3\dfrac{\dfrac{\sin kR}{kR}-\cos kR}{(kR)^2}}{(kR)^2}\right)$$

$$=\frac{\dfrac{kR-\dfrac{(kR)^3}{3!}+\cdots}{kR}-3\left(\dfrac{\dfrac{kR-\dfrac{(kR)^3}{3!}+\dfrac{(kR)^5}{5!}-\cdots}{kR}-(1-\dfrac{(kR)^2}{2!}+\dfrac{(kR)^4}{4!}-\cdots)}{(kR)^2}\right)}{(kR)^2} \tag{3.15c}$$

$$=-\frac{1}{15}$$

Subsequently, from (3.14b) and (3.15a) - (3.15c), it is concluded that:

$$\begin{aligned}\lim_{m\to n} G^{I}_{m,n_{i,j}} &= \frac{\eta_o}{4\pi} J_{j_n}\omega_n\left[k^2\left(\vec{a}_{i_m}\cdot\vec{a}'_{j_n}\right)\left[-1+\frac{2}{3}\right]-k^4\left(\vec{a}_i\cdot\vec{R}_{m,n}\right)\left(\vec{a}'_{j_n}\cdot\vec{R}_{m,n}\right)\frac{1}{15}\right]\\ &=\frac{\eta_o}{4\pi} J_{j_n}\omega_n\left[-\frac{1}{3}k^2\left(\vec{a}_{i_m}\cdot\vec{a}'_{j_m}\right)\right]\end{aligned} \tag{3.16}$$

In summary, (3.8) - (3.16) present the underlying Nyström formulation for the EFIE. It was observed that since G^I is regular, then the contribution due to G^I in the discrete integrand of (3.8) is regular and can be evaluated to high-order via numerical quadrature. Subsequently, these terms do not require local corrections. On the other hand, G^R is singular, and the terms of $G^R_{m,n_{i,j}}$ actually exhibit hypersingularities. Subsequently, these terms must be locally corrected to realize both a well-posed formulation and a formulation that yields high-order convergence. Furthermore, due to the hypersingularity of the integrand, this term will have to be manipulated such that the numerical integration is numerically tractable.

3.2 Locally Correcting G^R

3.2.1 Patch Based Local Corrections

The local corrections of the discrete kernel $G^R_{m,n_{i,j}}$ will be performed in a manner similar to that outlined by (2.6). Specifically, specialized quadrature rules will be developed such that the evaluation of (3.8) is exact for a given set of basis functions. Interestingly, only the contribution due to G^R will be locally corrected.

As outlined in Section 2, the local corrections are performed by first introducing a set of suitable basis functions that are distributed over *S*. This basis set will actually serve as a sample set of currents distributed on *S*. The field radiated by these currents will be calculated at the field point $\vec{r}_m$ on *S*. This will be calculated in two ways. The first is using the discrete kernel in (3.8) (with $G^R_{m,m_{i,j}} = 0$). The second will be using an *exact* integration of (3.6) for the kernel G^R. Since this expression cannot be evaluated in closed form, the *exact* integration is performed using an adaptive quadrature to a specified precision. The residual representing the difference between the exact integration and the discrete kernel is then computed for each basis function. This residual term, which appears on the right-hand-side of (2.6), will be used as the forcing function for the local correction terms.

Two classes of local correction operators can be used to correct the discrete kernel. The first is what is referred to as *patch-based* correction. The second is referred to as *entire-domain* correction. Patch based local corrections imply that the new quadrature rule represented by the local corrections is limited to the support of a patch. Thus, for each field point, a new quadrature rule is established for each patch. For the entire-domain approach, a new quadrature rule is established for a sufficiently large area surrounding the field point.

Patch-based local corrections restricts the support of the basis functions to that of a patch. Subsequently, this limits the support of the quadrature rule derived for each local correction. The advantage of the patch-based local correction is that the linear systems of equations needed to solve for the new quadrature weights are small and generally well conditioned. It also allows the use of orthogonal functions that lead to orthogonal matrices that are analytically solved. Another advantage is that the corrections rely on a local curvilinear coordinate system rather than a global coordinate system. This provides for a more robust solution for three-dimensional surfaces. The disadvantage is that this scheme can lead to asymmetries in the final impedance matrix, and if one is not careful can result in current discontinuities in the final solution.

On the other hand, entire-domain based local corrections utilize basis functions that are distributed over the entire surface *S*. The support of integration is then limited to being sufficiently large to reduce the residual error below a tolerable level of accuracy. One advantage of such a scheme is that current continuity is enforced by the basis functions. However, for three-dimensional surfaces, such a scheme is often limited to canonical geometries for which a global curvilinear coordinate system is easily derived. Furthermore, entire-domain schemes lead to large linear systems that are often very poorly conditioned.

In this report, the focus is limited to patch-based correction schemes. Entire domain schemes can be derived in similar manners - but without the bounded support of the integrations. The details of the corrections are provided below.

Each local correction is associated with a single field point $\vec{r}_m$. Thus, for a patch based scheme, only the row entries of $G_{m,n}$ associated with a single patch are corrected at a time. A two-dimensional basis set is introduced over each patch. Within the curvilinear coordinate system, the vector basis is introduced as:

$$\vec{J}(u^{1'},u^{2'}) = \frac{f_1^k(u^{1'},u^{2'})\vec{a}_1' + f_2^k(u^{1'},u^{2'})\vec{a}_2'}{\sqrt{g'}} \tag{3.17}$$

where k represents the order of the testing function, and the $\vec{a}_i'$ are the unitary vectors evaluated at $\left(u^{1'},u^{2'}\right)$. It is noted that the basis is normalized by the Jacobian such that the current basis is divergenceless. The vector current basis will serve as a sample current distributed over the patch. Subsequently, the field radiated by the current is calculated at $\vec{r}_m$ using exact integration and the discrete kernel. The local correction establishes a new quadrature rule which when operating on the current basis yields the residual error between the exact and discrete integrations. This is actually applied independently to each quadrant of the discrete kernel in (3.9). For example, consider quadrant (*i, j*). The quadrature rule operating on the *k*-th basis function is expressed as:

$$\begin{aligned}\sum_{n=1}^{N_q} \gamma_n \omega_n f_j^k(\vec{r}_n') = & -jk_o\eta_o \int_S \left(\vec{a}_i \cdot \vec{a}_j'\right) G^R(\vec{r}_m,\vec{r}') \frac{f_j^k\left(\vec{r}'\right)}{\sqrt{g'}}\, ds' \\ & - j\frac{\eta_o}{k_o}\vec{a}_i \cdot \nabla \int_S \left(\nabla G^R(\vec{r}_m,\vec{r}') \cdot \vec{a}_j' \frac{f_j^k\left(\vec{r}'\right)}{\sqrt{g'}}\right) ds' \\ & - \sum_{\substack{n=1 \\ n\neq m}}^{N_q} G^R_{m,n_{i,j}} f_j^k(\vec{r}_n')\omega_n \end{aligned} \tag{3.18}$$

where, $\vec{r}_m$ is the field point, and $\vec{r}_n'$ and ω_n are the abscissa and weights of the underlying quadrature rule and the patch being corrected, and γ_n are the new quadrature weights to be computed. The first two terms on the right-hand-side of (3.18) correspond to the exact integration of the convolution of the kernel with the basis functions $f_j^k(\vec{r})$, and the last term the numerical quadrature approximation of the convolution with $G^R_{m,n_{i,j}}$ defined in (3.14a). This procedure is repeated for K basis functions, leading to a linear system of equations:

$$\begin{pmatrix} \omega_1 f_j^1(\vec{r}_1) & \omega_2 f_j^1(\vec{r}_2) & \cdots & \omega_{N_q} f_j^1(\vec{r}_{N_q}) \\ \omega_1 f_j^2(\vec{r}_1) & \omega_2 f_j^2(\vec{r}_2) & \cdots & \omega_{N_q} f_j^2(\vec{r}_{N_q}) \\ \vdots & \vdots & \ddots & \vdots \\ \omega_1 f_j^K(\vec{r}_1) & \omega_2 f_j^K(\vec{r}_2) & \cdots & \omega_{N_q} f_j^K(\vec{r}_{N_q}) \end{pmatrix} \begin{pmatrix} \gamma_1 \\ \gamma_2 \\ \vdots \\ \gamma_{N_q} \end{pmatrix} = \begin{pmatrix} R_m^1 \\ R_m^2 \\ \vdots \\ R_m^K \end{pmatrix} \tag{3.19}$$

where R_m^k is the residual error resulting from the right-hand-side of (3.18) for the kth basis function $f_j^k(\vec{r})$. This is then solved for the vector γ_n. Subsequently, the product $\omega_n \gamma_n$ is then inserted in the appropriate entries of the *m*-th row of the local correction matrix in the (*i, j*) quadrant.

Once the local corrections are performed for the *m*-th row, then the impedance matrix is updated. Specifically, from (2.5) each quadrant is corrected as:

$$\overline{G}_{m,n_{i,j}} = G_{m,n_{i,j}} + L_{m,n_{i,j}}\,. \tag{3.20}$$

3.2.2 Evaluating the Self Patch

In the preceding section, the residual term on the right-hand-side of (3.19) requires the evaluation of the exact integral operator operating on the basis function. When the field point lies on the same patch as the basis function, the integrand will be hypersingular, as described in Section 2. Subsequently, the integral operator has to be modified such that the integral is numerically tractable. Specifically, the hypersingular terms arise from the gradient divergence of the real part of the Green's function. It is this term that will be manipulated. To this end, this term is first rewritten as:

$$\begin{aligned} \int_S \vec{a}_i \cdot \nabla\left(\left(\nabla G^R(\vec{r},\vec{r}\,')\right)\cdot \vec{J}(\vec{r}\,')\right) ds' &= -\int_S \vec{a}_i \cdot \nabla\left(\left(\nabla' G^R(\vec{r},\vec{r}\,')\right)\cdot \vec{J}(\vec{r}\,')\right) ds' \\ &= -\int_S \vec{J}(\vec{r}\,') \cdot \nabla'_{\|}\left(\vec{a}_i \cdot \nabla G^R(\vec{r},\vec{r}\,')\right) ds' \end{aligned} \tag{3.21}$$

where $\nabla G^R(\vec{r},\vec{r}\,') = -\nabla' G^R(\vec{r},\vec{r}\,')$, and $\nabla'_{\|}$ is tangential to the surface. Next, utilizing the vector identity $\nabla\cdot\left(\phi\vec{A}\right) = \phi\nabla\cdot\vec{A} + \vec{A}\cdot\nabla\phi$, the right-hand-side of (3.21) is rewritten as

$$= -\int_S \nabla'_{\|} \cdot \left[\vec{J}(\vec{r}\,') \left(\vec{a}_i \cdot \nabla G^R(\vec{r},\vec{r}\,') \right) \right] ds' + \int_S \nabla'_{\|} \cdot \vec{J}(\vec{r}\,') \left(\vec{a}_i \cdot \nabla G^R(\vec{r},\vec{r}\,') \right) ds' \tag{3.22}$$

It is then realized that the first term on the right-hand-side of (3.22) can be rewritten using the divergence theorem for open surfaces [2] as:

$$\int_S \nabla'_{\|} \cdot \left[\vec{J}(\vec{r}\,') \left(\vec{a}_i \cdot \nabla G^R(\vec{r},\vec{r}\,') \right) \right] ds' = \oint_C \left(\hat{e}' \cdot \vec{J}(\vec{r}\,') \right) \left(\vec{a}_i \cdot \nabla G^R(\vec{r},\vec{r}\,') \right) dl' \tag{3.23}$$

where C is the closed contour bounding the open surface S, and $\hat{e}'$ is the outward normal to the contour that is also tangential to the surface (i.e., $\hat{e}'dl' = d\vec{l}\,' \times \hat{n}$). The second-term on the right-hand-side of (3.22) is rewritten as:

$$\int_S \nabla'_{\|} \cdot \vec{J}(\vec{r}\,') \left(\vec{a}_i \cdot \nabla G^R(\vec{r},\vec{r}\,') \right) ds' = \int_S \nabla G^R(\vec{r},\vec{r}\,') \cdot \left[\vec{a}_i \nabla'_{\|} \cdot \vec{J}(\vec{r}\,') \right] ds' \tag{3.24}$$

This is then rewritten as:

$$= \int_S \nabla G^R(\vec{r},\vec{r}\,') \cdot \left[\vec{a}_i \nabla'_{\|} \cdot \vec{J}(\vec{r}\,') - \vec{K} \right] ds' + \int_S \nabla G^R(\vec{r},\vec{r}\,') \cdot \vec{K}' ds' \tag{3.25}$$

where, $\vec{K}'$ is a vector defined by

$$\vec{K}' = \vec{a}_i' \left[\nabla'_{\|} \cdot \vec{J}(\vec{r}\,') \Big|_{\vec{r}\,'=\vec{r}} \right] = \frac{\vec{a}_i'}{\sqrt{g'}} \chi \,. \tag{3.26}$$

The constant χ is chosen such that at the singular point $\vec{K}' = \vec{a}_i \nabla'_{\|} \cdot \vec{J}(\vec{r}\,')$. Thus,

$$\chi = \sqrt{g} \left[\nabla'_{\|} \cdot \vec{J}(\vec{r}\,') \Big|_{\vec{r}\,'=\vec{r}} \right]. \tag{3.27}$$

Thus, choosing $\vec{K}'$ according to (3.26) and (3.27), the integrand of the first integral in (3.25) becomes regular. This occurs because the cancellation of $\vec{a}_i \nabla'_{\|} \cdot \vec{J}(\vec{r}\,')$ cancels out one of two poles of $\nabla G^R(\vec{r},\vec{r}\,')$. This leaves an integrand with a single pole that can be integrated numerically.

The second term in (3.25) must still be manipulated into an integrable form. To this end:

$$\begin{aligned}
\int_S \nabla G^R(\vec{r},\vec{r}\,') \cdot \vec{K}' ds' &= -\int_S \nabla' G^R(\vec{r},\vec{r}\,') \cdot \frac{\vec{a}_i'}{\sqrt{g'}} \chi ds' \\
&= -\int_S \chi \left(\frac{\vec{a}_i'}{\sqrt{g'}} \cdot \nabla'_{\|} G^R(\vec{r},\vec{r}\,') \right) ds' \qquad (3.28) \\
&= -\int_S \chi \left[\nabla'_{\|} \cdot \left(\frac{\vec{a}_i'}{\sqrt{g'}} G^R(\vec{r},\vec{r}\,') \right) - G^R(\vec{r},\vec{r}\,') \nabla'_{\|} \cdot \frac{\vec{a}_i'}{\sqrt{g'}} \right] ds'
\end{aligned}$$

It can be shown that $\nabla'_{\|} \cdot \frac{\vec{a}'_i}{\sqrt{g'}} = 0$. Thus, applying the open surface divergence theorem:

$$\int_S \nabla G^R(\vec{r},\vec{r}\,') \cdot \vec{K}'ds' = -\chi \oint_C \hat{e}' \cdot \frac{\vec{a}'_i}{\sqrt{g'}} G^R(\vec{r},\vec{r}\,')dl' \tag{3.29}$$

Finally, from (3.21)-(3.29),

$$\begin{aligned} \vec{a}_i \cdot \nabla \int_S \left(\nabla G^R(\vec{r},\vec{r}') \cdot \vec{J}(\vec{r}')\right) ds' &= +\int_S \nabla G^R(\vec{r},\vec{r}') \cdot \left[\vec{a}_i \nabla'_{\|} \cdot \vec{J}(\vec{r}') - \vec{K}\right] ds' \\ &\quad - \oint_C \left(\hat{e}' \cdot \vec{J}(\vec{r}')\right)\left(\vec{a}_i \cdot \nabla G^R(\vec{r},\vec{r}')\right) dl' \\ &\quad - \chi \oint_C \hat{e}' \cdot \frac{\vec{a}'_i}{\sqrt{g'}} G^R(\vec{r},\vec{r}')dl' \end{aligned} \tag{3.30}$$

The expression in (3.30) can now be used to evaluate the right-hand-side of (3.18). To this end, define:

$$\begin{aligned} \bar{G}^R_{m,k_{i,j}} &= -jk_o\eta_o \int_S \left(\vec{a}_i \cdot \vec{a}'_j\right) G^R(\vec{r}_m,\vec{r}') f^k_j\left(\vec{r}'\right) ds' \\ &\quad - j\frac{\eta_o}{k_o} \vec{a}_i \cdot \nabla \int_S \left(\nabla G^R(\vec{r}_m,\vec{r}') \cdot \vec{a}'_j f^k_j\left(\vec{r}'\right)\right) ds' \end{aligned} \tag{3.31}$$

where the second term on the right-hand-side of (3.31) is to be replaced with (3.30).

The above integrals are performed using an adaptive quadrature. The leading singularity is *1/R*, which is numerically tractable. To accelerate the integration, a Duffy transform is used [8]. To this end, the patch is first subdivided into triangles with sharing a common vertex at $\vec{r}_m$. The Duffy transform simply defines the triangle as a quadrilateral with two vertices shared at the common vertex at $\vec{r}_m$. Subsequently, the Jacobian goes to zero at this vertex. This greatly accelerates the adaptive quadrature.

4. Application of the LCN Method to the MFIE

4.1 The MFIE

An integro-differential operator magnetic field integral equation (MFIE) can be used to solve for the induced equivalent surface currents providing the PEC body is a closed surface. The MFIE is applied on the surface of the body through the simple boundary relationship:

$$\hat{a}_n \times \left(\vec{H}^{tot}\Big|_{S^+} - 0|_{S^-} \right) = \vec{J} \tag{4.1}$$

where $\hat{a}_n$ is the outward normal, S^+ indicates the closed surface just outside of S, and S^- the closed surface just inside of S. Next, a test vector $\vec{a}_i$ that is tangential to S is introduced. Subsequently, (4.1) is modified as:

$$\begin{aligned} &\vec{a}_i \cdot \left(\hat{a}_n \times \hat{a}_n \times \left(\vec{H}^{tot}\Big|_{S^+} \right) \right) = \vec{a}_i \cdot \left(\hat{a}_n \times \vec{J} \right) \\ &\Rightarrow -\vec{a}_i \cdot \vec{H}^{tot}\Big|_{S^+} = \vec{a}_i \cdot \left(\hat{a}_n \times \vec{J} \right) \end{aligned} \tag{4.2}$$

Finally, letting $\vec{H}^{tot} = \vec{H}^s + \vec{H}^{inc}$, and realizing that

$$\vec{H}^s(\vec{r}) = \oint_S \nabla \times G(\vec{r},\vec{r}')\vec{J}(\vec{r}')ds' \tag{4.3}$$

leads to the MFIE:

$$-\vec{a}_i \cdot \vec{H}^{inc}(\vec{r}) = \vec{a}_i \cdot \left(\hat{a}_n \times \vec{J}(\vec{r}) \right) + \vec{a}_i \cdot \oint_S \nabla \times G(\vec{r},\vec{r}')\vec{J}(\vec{r}')ds' \tag{4.4}$$

where, $\vec{r} \in S^+$.

The surface current density is again assumed to be expanded in terms of two independent vectors chosen to be the unitary vectors defining the surface as:

$$\vec{J}(\vec{r}) = \frac{\vec{a}_1 J_1 + \vec{a}_2 J_2}{\sqrt{g}}. \tag{4.5}$$

where $\sqrt{g}$ is the Jacobian and $\vec{a}_i$ $(i = 1,2)$ are the unitary vectors at $\vec{r}$. It is noted that from (3.4) and (3.5), it can be shown that

$$\sqrt{g} = \left| \vec{a}_1 \times \vec{a}_2 \right|. \tag{4.6}$$

Subsequently, from (4.5) and (4.6), the first term on the right-hand-side of (4.4) is evaluated as:

$$\vec{a}_i \cdot \left(\hat{a}_n \times \vec{J}(\vec{r}) \right) = \kappa_i = \begin{cases} -J_2, & i = 1 \\ J_1, & i = 2 \end{cases} \tag{4.7}$$

Next, the integral on the right-hand-side of (4.4) is analyzed. To this end, it is realized that:

$$\begin{aligned}\nabla\times\left(\vec{J}\left(\vec{r}'\right)G\left(\vec{r},\vec{r}'\right)\right) &= G\left(\vec{r},\vec{r}'\right)\nabla\times\vec{J}\left(\vec{r}'\right)-\vec{J}\left(\vec{r}'\right)\nabla G\left(\vec{r},\vec{r}'\right)\\ &= -\vec{J}\left(\vec{r}'\right)\nabla G\left(\vec{r},\vec{r}'\right)\\ &= \vec{J}\left(\vec{r}'\right)\nabla' G\left(\vec{r},\vec{r}'\right)\end{aligned} \qquad . \tag{4.8}$$

where ∇' implies the gradient in the primed coordinate system. Next, it is seen that:

$$\nabla' G\left(\vec{r},\vec{r}'\right) = -\frac{\vec{R}}{R}\frac{\partial}{\partial R}\left[G^R(R)+jG^I(R)\right]. \tag{4.9}$$

where $\vec{R}=\vec{r}-\vec{r}'$, $R=\left|\vec{R}\right|$, and G^R and G^I are defined in (3.10). This is explicitly written as:

$$\nabla' G\left(\vec{r},\vec{r}'\right) = -\frac{k^3}{4\pi}\vec{R}\left[K^R(R)+jK^I(R)\right]. \tag{4.10}$$

where,

$$K^R(R) = \frac{kR\sin(kR)+\cos(kR)}{(kR)^3} \tag{4.11}$$

and

$$K^I(R) = \frac{\cos(kR)-\dfrac{\sin(kR)}{kR}}{(kR)^2}. \tag{4.12}$$

Again, it is seen that the contribution from the imaginary part of the Green's function is regular, and that from the real part is singular.

The expressions from (4.10) through (4.12) can then be used within (4.4). Upon inspection, it becomes obvious that the integral over the real term $K^R(R)$ requires the principal value integral. Specifically, it is assumed that $\vec{r}$ is on S^+. However, $K^R(R)$ is hypersingular on S^+. Thus, this integral must be manipulated. To this end, define $\vec{r}$ is on S^+ as:

$$\vec{r} = \vec{r}_S + \hat{a}_n\varepsilon\,. \tag{4.13}$$

where $\vec{r}_S$ is on *S*, $\hat{a}_n$ is the unit normal to *S* at $\vec{r}_S$, and ε is the projection between S^+ and *S* ($\varepsilon > 0$). Then, one can also define:

$$\vec{R} = \vec{r}-\vec{r}' = \vec{r}_S-\vec{r}'+\hat{a}_n\varepsilon = \vec{R}_s+\hat{a}_n\varepsilon\,. \tag{4.14}$$

where in the limit that $\varepsilon\to 0$, $\left|\vec{R}\right|\approx\left|\vec{R}_s\right|$. Then, from (4.7), (4.10), and (4.14), (4.4) can be rewritten as:

$$
\begin{aligned}
-\vec{a}_i \cdot \vec{H}^{inc}(\vec{r}) = \kappa_i &+ \frac{k^3}{4\pi}\int_S \vec{R}_s \cdot \left(\vec{a}_i \times \vec{J}(\vec{r}')\right)\left(K^R(R) - jK^I(R)\right)\sqrt{g'}ds' \\
&+ \lim_{\varepsilon \to 0}\frac{k^3}{4\pi}\int_{S_\varepsilon} \hat{a}_n \varepsilon \cdot \left(\vec{a}_i \times \vec{J}(\vec{r}')\right)\left(K^R(R) - jK^I(R)\right)\sqrt{g'}ds'
\end{aligned}
\tag{4.15}
$$

where κ_i is given by (4.7), and the second term on the right-hand-side is a principal value integral over the small surface S_ε encircling the field point. Focusing on the first term on the right-hand-side of (4.15), the integrand involving K^I is regular. The integrand involving K^R is singular and integrable. Specifically, from (4.11), K^R has a $1/R^3$ singularity. However, in the limit that $R \to 0$, both $\vec{R}_s \to 0$ and the dot product $\vec{R}_s \cdot \vec{a}_i \times \vec{J}(\vec{r}') \to 0$. The latter condition arises since the cross product is normal to the surface at the field point, and $\vec{R}_s$ is tangential. Thus, the integrand will have a $1/R$ singularity, which is integrable.

Next, the principal value integral is treated. Initially, since K^I is regular and bounded as $R \to 0$, the integral of this term will tend to 0 as $\varepsilon \to 0$. However, based on the previous arguments, since the dot product $\hat{a}_n \cdot \left(\vec{a}_i \times \vec{J}(\vec{r}')\right)$ is not zero in the limit $R \to 0$, the integrand is hypersingular. Let us consider this term further. For simplification, consider the case when $\vec{a}_i = \vec{a}_1$. Given $\vec{J}(\vec{r}')$ defined by (4.5), then, it is seen that:

$$
\lim_{\vec{r} \to \vec{r}'} \hat{a}_n \cdot \left(\vec{a}_1 \times \frac{\left(\vec{a}_1' J_1 + \vec{a}_2' J_2\right)}{\sqrt{g'}}\right) = \hat{a}_n \cdot \left(\vec{a}_1 \times \vec{a}_2\right)\frac{J_2}{\sqrt{g}} = J_2 . \tag{4.16}
$$

Since the contribution due to K^I is zero, the principal value integral in (4.15) can be rewritten using (4.11) and (4.16) as:

$$
\mathrm{PVI} = \lim_{\varepsilon \to 0}\frac{k^3}{4\pi}\varepsilon J_2 \int_{S_\varepsilon}\left(\frac{kR\sin(kR) + \cos(kR)}{(kR)^3}\right)\sqrt{g'}ds' \tag{4.17}
$$

In the region near the field point, R is assumed to be very small. Subsequently, small argument aproximations for the trigonometric functions can be applied, where:

$$
\begin{aligned}
\sin(kR) &\approx kR + O\left((kR)^3\right) \\
\cos(kR) &\approx 1 + O\left((kR)^2\right)
\end{aligned}
\tag{4.18}
$$

Next, the surface S_ε is approximated by a small disk of radius $\Delta\rho$ centered about the field point. Subsequently, the principal value integral is written as:

$$\text{PVI} = \lim_{\varepsilon\to 0}\frac{k^3}{4\pi}\varepsilon J_2\left[\int_{\rho=0}^{\Delta\rho}\int_{\phi=0}^{2\pi}\left(\frac{(kR)^2}{(kR)^3}+\frac{1}{(kR)^3}\right)\rho\, d\phi\, d\rho\right] \tag{4.19}$$

Next, let $R=\sqrt{\rho^2+\varepsilon^2}$, which leads to:

$$\begin{aligned}\text{PVI} &= \lim_{\varepsilon\to 0}\frac{k^3}{2}\varepsilon J_2\left[\int_{\rho=0}^{\Delta\rho}\left(\frac{1}{k\sqrt{\rho^2+\varepsilon^2}}+\frac{1}{k^3\left(\rho^2+\varepsilon^2\right)^{\frac{3}{2}}}\right)\rho\, d\rho\right]\\ &= \lim_{\varepsilon\to 0}\frac{k^3}{2}\varepsilon J_2\left[\frac{\varepsilon^2-\varepsilon\sqrt{\Delta\rho^2+\varepsilon^2}}{k}+\frac{-\varepsilon+\sqrt{\Delta\rho^2+\varepsilon^2}}{k^3\varepsilon\sqrt{\Delta\rho^2+\varepsilon^2}}\right]\\ &= \frac{k^3}{2}J_2\left[0+\frac{1}{k^3}\right]=\frac{1}{2}J_2\end{aligned} \tag{4.20}$$

Similarly, for $i = 2$, it can be shown that the PVI = $-\frac{1}{2}J_1$. Finally, from (4.20) and (4.15), the MFIE is expressed as:

$$-\vec{a}_i\cdot\vec{H}^{inc}(\vec{r})=\frac{\kappa_i}{2}+\frac{k^3}{4\pi}\int_S\vec{R}_s\cdot\left(\vec{a}_i\times\vec{J}(\vec{r}')\right)\left(K^R(R)-jK^I(R)\right)\sqrt{g'}ds' \tag{4.21}$$

4.2 The Locally Corrected Nyström Formulation of the MFIE

The MFIE will also be analyzed using the locally corrected Nyström scheme. To this end, the surface S is discretized into P patches. As for the EFIE, it is assumed that the patches are curvilinear and provide a high-order description of the surface geometry. Subsequently, (4.21) is approximated by numerical quadrature by introducing a quadrature rule for each patch. Then, sampling the field point at abscissa point $\vec{r}_m$, the Nyström approximation of (4.21) is:

$$\begin{aligned}-\vec{a}_{i_m}\cdot\vec{H}^{inc}(\vec{r}_m)&=\frac{\kappa_i}{2}\delta_{m,n}\\ &+\frac{k^3}{4\pi}\sum_{p=1}^{P}\sum_{n=1}^{N_q}\vec{R}_{m,n}\cdot\left(\vec{a}_{i_m}\times\vec{J}(\vec{r}_n)\right)\left(K^R\left(R_{m,n}\right)-jK^I\left(R_{m,n}\right)\right)\omega_n\sqrt{g_n}\end{aligned} \tag{4.22}$$

where, $\vec{R}_{m,n}=\vec{r}_m-\vec{r}_n$, $R_{m,n}=\left|\vec{R}_{m,n}\right|$, and $\delta_{m,n}$ is the Kronecker delta function.

Thus, a discrete kernel is defined as

$$G_{m,n_{i,j}}=G^R_{m,n_{i,j}}+G^I_{m,n_{i,j}} \tag{4.23}$$

where, the *m,n*th entries in quadrant (*i, j*) of the discrete kernel is:

$$G^R_{m,n_{i,j}} = \frac{k^3}{4\pi}\vec{R}_{m,n}\cdot\left(\vec{a}_{i_m}\times\vec{a}'_{j_n}\right)\left(K^R\left(R_{m,n}\right)\right)\omega_n \tag{4.24a}$$

$$G^I_{m,n_{i,j}} = -j\frac{k^3}{4\pi}\vec{R}_{m,n}\cdot\left(\vec{a}_{i_m}\times\vec{a}'_{j_n}\right)\left(K^I\left(R_{m,n}\right)\right)\omega_n \tag{4.24b}$$

where, $\vec{a}_{i_m}$ is a unitary vector evaluated at the field point $\vec{r}_m$ and $\vec{a}'_{j_n}$ is a unitary vector evaluated at the source point $\vec{r}_n$.

In the limit that $m = n$ (i.e., $R_{m,m} \to 0$) K^I is bounded, as seen from (4.12). Furthermore, in this limit, the dot product is zero, and $\vec{R}_{m,n} \to 0$. Subsequently, $G^I_{m,m_{i,j}} = 0$. On the other hand, $G^R_{m,m_{i,j}}$ is infinite in value due to the singularity of K^R. Thus, $G^R_{m,n_{i,j}}$ must be locally corrected.

The local corrections can be carried out in the same fashion as outlined in Section 3.2.1. One advantage of the MFIE over the EFIE is that the level of singularity of $G^R_{m,m_{i,j}}$ is simply *1/R*. Subsequently, the exact integration in (4.21) can be carried out numerically in an efficient manner using adaptive quadrature and the Duffy transform [8].

5. Numerical Validation of the Nyström Solution

The locally corrected Nyström (LCN) methods presented in this paper report been applied successfully to the electromagnetic scattering analysis of PEC bodies. This section summarizes some of these results. The focus of this study is on the accuracy and convergence characteristics of LCN method when applied to the computation of the RADAR cross section (RCS) of PEC objects. Initially smooth bodies are studied. Then, the method is applied to open structures with edge singularities.

The error convergence of the LCN method will specifically be presented by studying the root mean square error (RMS) in the RCS as the level of discretization is modified. The RMS error is computed relative to a known reference solution which is either obtained analytically for canonical geometries or numerically through a LCN solution with a very high level of discretization. Specifically, given the RCS computed over a sphere in the far field, the RMS error is estimated as:

$$\text{RMS Error} = \sqrt{\frac{\int_{\phi=0}^{2\pi}\int_{\theta=0}^{\pi} |RCS_{ref}(\theta,\phi) - RCS_{LCN}(\theta,\phi)|^2 \sin\theta d\theta d\phi}{\int_{\phi=0}^{2\pi}\int_{\theta=0}^{\pi} |RCS_{ref}(\theta,\phi)|^2 \sin\theta d\theta d\phi}} \tag{5.1}$$

where θ and ϕ are the observation angles, $RCS_{ref}(\theta,\phi)$ is the reference RCS computed analytically (if possible) or numerically to high precision, and $RCS_{LCN}(\theta,\phi)$ is the RCS computed via the LCN method.

The first example illustrated is that of a PEC sphere. The study of this problem is of interest because of its smooth geometry and the fact that the RCS can be calculated analytically using a Mie series solution. The sphere was discretized using curvilinear quadrilateral patches that exactly modeled the curvature of the sphere. At the poles of the sphere, the quadrilateral essentially becomes triangular in shape as two vertices will coincide. The quadrature rule for each sphere was then determined via a product rule of one-dimensional Gauss-Legendre quadratures. Orthogonal patch based testing functions were used for the local corrections. The number of testing functions used was equal to the number of quadrature points, resulting in an orthogonal test matrix.

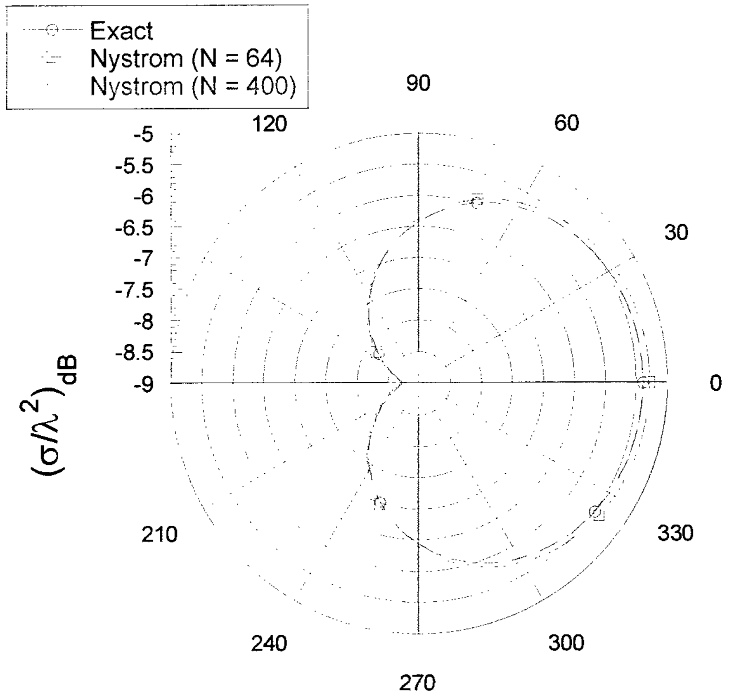

Fig. 5.1 RCS of a PEC sphere versus θ computed in the $\phi = 90°$ plane when illuminated by an x-directed electric field propagating along the negative z-direction with radius defined by $k_o a = 1$. Results from the locally corrected Nyström method with a total number of unknowns equal to 64 and 400 and an exact MIE series solution are illustrated.

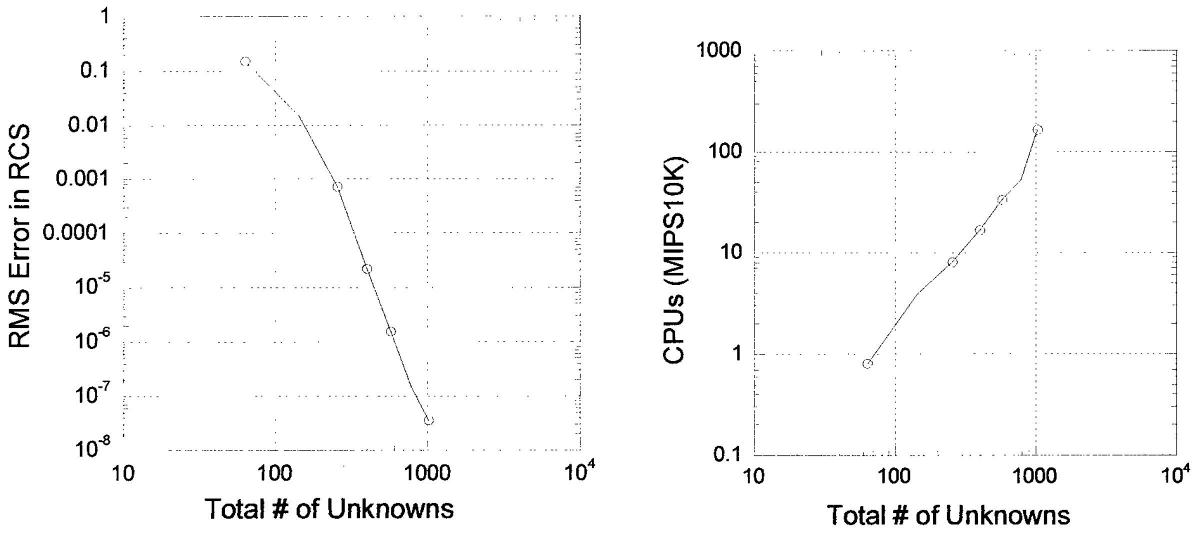

(a) (b)

Fig. 5.2 RMS error in the RCS for the LCN solution of the MFIE for the scattering by the $k_o a = 1$ PEC sphere as the quadrature order is increase. (a) RMS Error relative to the Mie series solution, (b) CPUs required to complete the computation on a MIPS R10,000 processor.

The sphere is assumed to have a radius a such that $k_0 a = 1$, where k_0 is the free space wavenumber. The sphere was illuminated by a plane wave traveling in the negative z-direction. The sphere was discretized using 8 quadrilateral patches (i.e., one patch per octant). The RCS was then computed as the quadrature order was increased. Figure 5.1 illustrates the RCS computed by the LCN method for two levels of discretization. The first used 4 quadrature points per patch (2 along each linear direction), which resulted in a total of 64 unknowns. The second assumed 25 quadrature points per patch (5 along each linear direction), resulting in a total of 400 unkowns. These results are compared to the exact Mie series solution.

The case with 4 quadrature points per patch has an error of roughly 0.2 dB in the backscatter region ($\theta = 0$). The 25-quadrature point per patch case is indiscernible from the exact solution on this graph.

The RMS error in the RCS was then calculated as a function of the number of degrees of freedom. These results are illustrated in Fig. 5.2(a), while the CPU time recorded for these simulations on a MIPS R10,000 processor is illustrated in Fig. 5.2(b). For these calculations, the degrees of freedom were simply increased by increasing the quadrature order per patch. Subsequently, on a log-log scale, the RMS error recorded in Fig. 5.2(a) is increasing in slope as the quadrature order is increased. This clearly shows that the Nyström scheme realizes exponential convergence. The case of $N = 256$ realizes 4 digits of accuracy, requiring only 8 CPU-seconds to compute, which is more than sufficient for engineering accuracy.

As demonstrated by the previous example, the LCN method yields high-order convergence for the RCS computation of closed smooth bodies (More extensive studies of this can be found in [2]). The question that arises is how applicable is the LCN for analyzing the RCS of surfaces with edge singularities. Specifically, when modeling geometries with edge singularities, a high-order solution can only be achieved if the surface current density can be represented to high order by the underlying quadrature rule. Thus, standard Gauss-Legendre quadrature would not provide high-order convergence, unless the discretization were refined in an appropriate manner near the edge. This would lead to an unnecessary increase in the number of degrees of freedom and the condition number of the impedance matrix. A more viable alternative is to introduce specialized quadrature rules that implicitly integrate the singular behavior to high order. Such quadrature rules have been successfully implemented for sharp edges on thin sheets in two and three dimensions [3, 9, 10]. It was shown for two-dimensional geometries, that a high-order representation can be realized using specialized quadrature rules [3]. As an example, consider the edge currents of a flat plate. The normal edge current are $\propto x^{1/2}$, and the tangential currents are $\propto x^{-1/2}$, where x is the distance from the edge. In three-dimensions this current can be integrated to high order using a Gauss-Jacobi quadrature rule [11].

The local corrections require the choice of a suitable basis $f_i^k(u^1,u^2)$ to be distributed over Ω. In this work, orthogonal subdomain functions representing the underlying quadrature rules are assumed. Specifically, for a quadrilateral cell, $f_i^k(u^1,u^2)$ is equal to the product of two one-dimensional Jacobi polynomials:

$$f_i^k\left(u^1,u^2\right)=P_{k_1}^{\alpha_1,\beta_1}\left(u^1\right)P_{k_2}^{\alpha_2,\beta_2}\left(u^2\right) \tag{17}$$

where $P_k^{\alpha,\beta}(u)$ is the *k*-th order Jacobi polynomial, (u^1,u^2) are the parametric coordinates for the cell with each defined over the range (-1,+1). For smooth patches without an edge singularity, α and β are chosen to be 0, realizing that $P_k^{0,0}(u)$ is equal to the *k*-th order Legendre Polynomial.

This choice of functions has a number of advantages. Initially, the local corrections can be efficiently performed on a cell by cell basis. Secondly, if appropriately scaled, the matrix resulting on the left-hand-side of (6) is orthogonal and the matrix can be diagonalized analytically. Finally, with the use of Jacobi polynomials, α and β can be appropriately selected such that singular currents are represented to high-order.

As an example, consider the finite strip array illuminated by a uniform plane wave illustrated in Fig. 5.3. The bistatic RCS for this array was computed using both the LCN and a commercially available method of moment (MoM) simulator (Zeland *IE3D*). For the LCN simulation, each strip was discretized into 5 rectangular cells, each being $0.25\lambda_o \times 2\lambda_o$ in dimension. The discretization was then refined by increasing the quadrature order. The MoM solution employed rectangular cells with roof top basis functions. Special edge cells were also included to improve the edge-current representation. The MoM discretization was refined by increasing the number of patches. The strip array was illuminated by a uniform plane wave incident from the broad side as illustrated in Fig. 5.3. The RCS in the $\phi = 0°$ plane as computed by both a MoM simulation with over 3000 unknowns and the LCN method with1080 unknowns is illustrated in Fig. 5.4. Excellent agreement is realized in this cross-section.

The root-mean-square (RMS) error in the RCS was then calculated for each technique as a function of the discretization level. These results are presented in Fig. 5.4. The error convergence realized by the MoM solution is only first-order. In fact, to realize 1 % error for this problem, the LCN method requires roughly one-fourth of the computational resources as the low-order MoM solution. Obviously for errors < 1 %, the LCN requires only a modest increase in resources. Whereas, it is unreasonable to expect better than 1 % accuracy from the low-order MoM solution. This demonstrates the specific advantage of the high-order scheme that increased orders of accuracy can be realized with only modest increase in the computational resources.

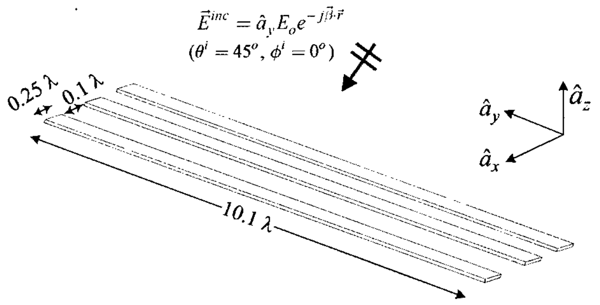
$\vec{E}^{inc} = \hat{a}_y E_o e^{-j\vec{\beta}\cdot\vec{r}}$
$(\theta^i = 45^o, \phi^i = 0^o)$
0.25 λ
0.1 λ
10.1 λ
$\hat{a}_y$
$\hat{a}_z$
$\hat{a}_x$

Fig. 5.3 Finite array of thin PEC strips in free space

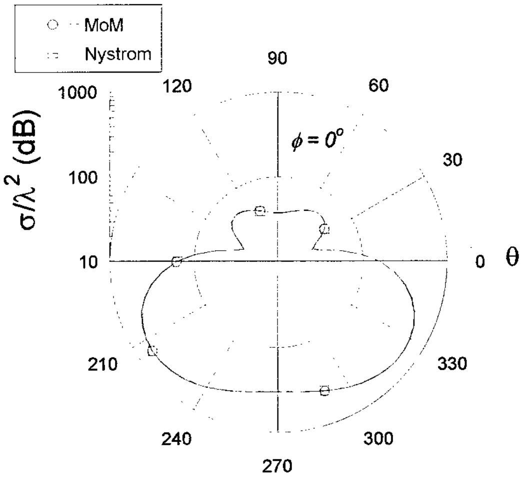

Fig. 5.4 Bistatic RCS of the finite strip array computed via the Nyström method.

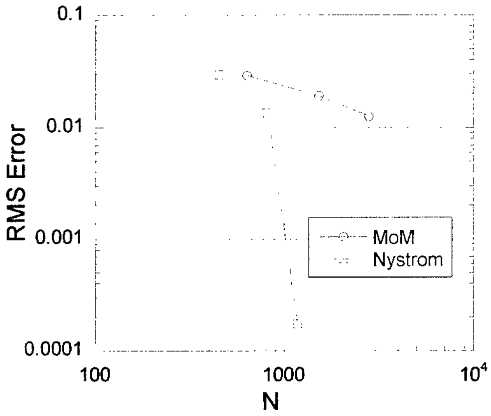

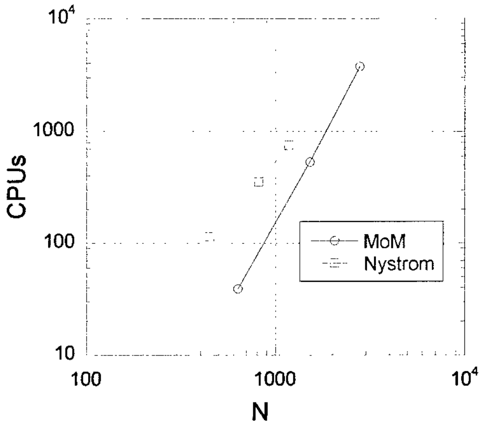

Fig. 5.5 RMS Error in the RCS versus *N* for both MoM and Nyström solutions.

Fig. 5.6 CPU time (in seconds) versus *N* for the MoM and the Nyström solutions.

The CPU times for the simulations in Fig. 5.5 were also recorded. For this calculation, the LCN solution was performed on a MIPS R10000 180 MHz processor with 1 Mb cache. The MoM solution was performed on a 350 MHz Pentium III PC. Thus, one cannot compare directly the CPU times. However, one can compare the rate of increase of the CPU time with the rate of error convergence. Specifically, the MoM simulation is linearly converging as the CPU time is increasing as $O\left(N^3\right)$. On the other hand, the LCN simulation is exponentially converging as the CPU time is increasing as $O\left(N^2\right)$ as the matrix fill dominates the computation as compared to the factorization.

The final example illustrated in this report is the scattering by a PEC hemisphere. The hemisphere has a radius defined again as $k_o a = 1$. This problem poses a particular challenge that the geometry is curved and it contains an edge singularity. The structure is discretized using curvilinear quadrilateral patches as used for the spherical scatterer. As with the strip study, Gauss-Jacobi quadrature is defined for patches containing an edge singularity and Jacobi polynomials are used for the basis functions for these patches as well. It is realized that since the surface is non-planar, that the singular behavior is not modeled exactly by the quadrature rule. Neverthless, it is anticipated that the rate of convergence will be still superior to that obtained using straight Gauss-Legendre quadrature.

A simplified geometry for the hemisphere is illustrated in Fig. 5.7. It is noted that the discretization and shading are an artifact of the imaging software and do not represent any physical meaning. The hemisphere was illuminated by an incident plane wave as illustrated in Fig. 5.7. The RCS computed in the $\phi = 0^\circ$ plane is illustrated in Fig. 5.8. The RCS was computed both using a MoM solution (Zeland *IE3D*) and the LCN method. The convergence in the RCS as a function of the discretization is illustrated in Fig. 5.9. For this study, the base discretization consisted of eight curvilinear patches that exactly modeled the surface curvature. To this end, there were two patches along the theta-direction (or zenith), and four along the phi-direction (or azimuthal). The number of quadrature points was then increased from 4 points per patch to 49 points per patch. The reference solution for the RMS error calculation was a more finely discretized solution with 12 patches and 81 points per patch.

Observing Fig. 5.9, it is seen that the RMS error is not demonstrating high-order convergence. The convergence is still more rapid than that expected for a low order method. However, it is not exponentially converging as the previous cases. It is anticipated that this is due to the fact that the edge singularity is not being modeled exactly by the Jacobi polynomial. However, since the edge behavior is better approximated than using a Gauss-Legendre quadrature rule, the convergence is still improved.

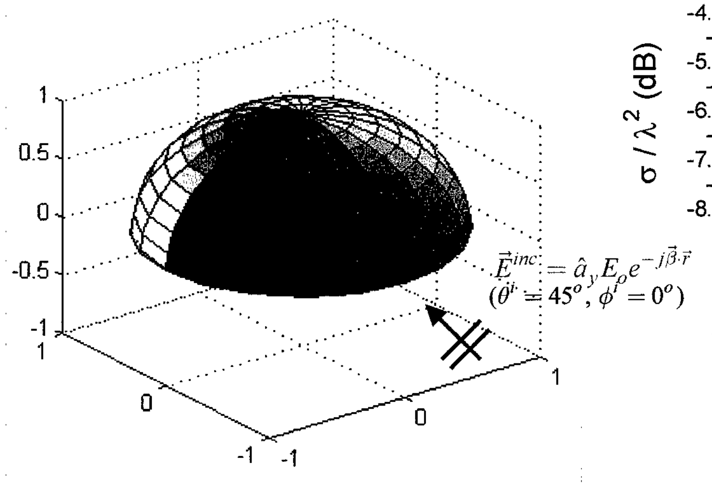
1
0.5
0
-0.5
-1
1
0
-1
-1
0
1
$\vec{E}^{inc} = \hat{a}_y E_o e^{-j\vec{\beta}\cdot\vec{r}}$
$(\theta^i = 45^o, \phi^i = 0^o)$

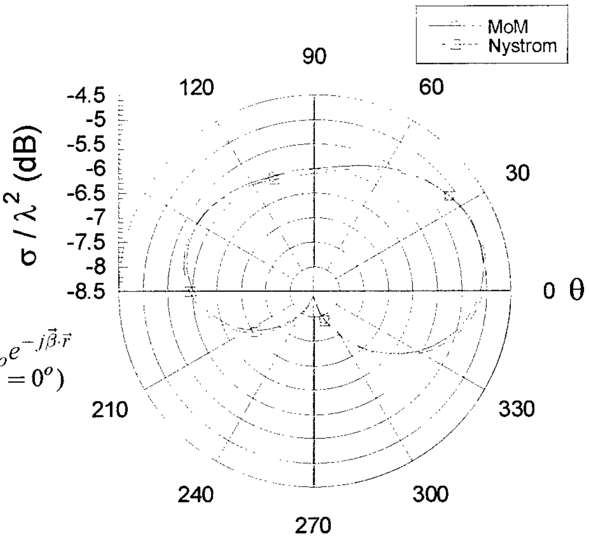

Fig. 5.7 Plane wave illumination of a PEC hemisphere $k_o a = 1$.

Fig. 5.8 RCS of the PEC Hemisphere versus θ in the $\phi = 0$ plane.

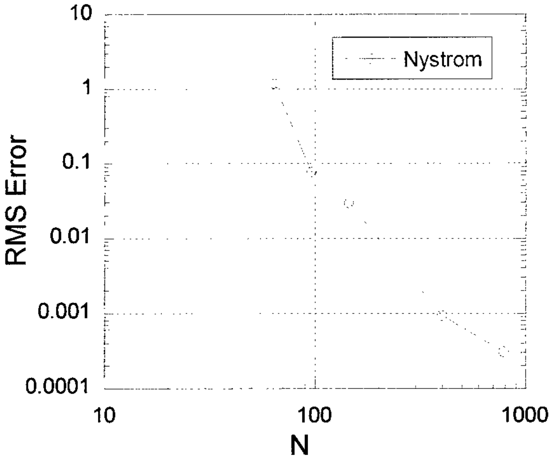

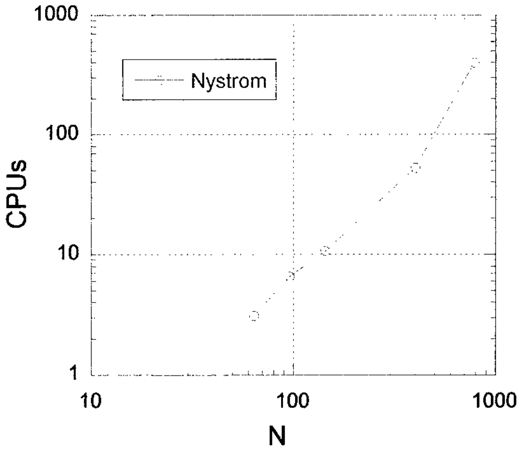

Fig. 5.9 Error convergence of the LCN solution of the scattering by the PEC hemisphere.

Fig. 5.10 CPU time for the calculations in Fig. 5.9.

6. Multilayered Green's function Computation

6.1 The MPIE

The Nyström scheme presented in the previous sections has been developed for the free-space Green's function. This is a necessary step in the development of this program. However, the ultimate goal is to apply the Nyström method to the solution of printed circuits in a layered media. To this end, the Nyström scheme will be applied to the mixed potential integral equation (MPIE) form of the EFIE. Specifically, (3.6) is rewritten as:

$$-\vec{a}_i \cdot \vec{E}^{inc} = -jk_o\eta_o \int_S \vec{a}_i \cdot \bar{\bar{G}}_A(\vec{r},\vec{r}') \cdot \vec{J}(\vec{r}')ds' + \vec{a}_i \cdot \nabla \int_S G_q(\vec{r},\vec{r}')\left(\nabla \cdot \vec{J}(\vec{r}')\right)ds' \qquad (6.1)$$

where $\bar{\bar{G}}_A$ is the dyadic Green's function representing the magnetic vector potential and G_q is the scalar potential for the layered medium.

In general, the Green's function in a layered media is not known in closed form, but is actually computed numerically [12]. The most computationally intensive component of this is the computation of Sommerfeld integrals that arise for both the magnetic vector and electric scalar potentials. For the Nyström simulation, it is imperative that this integrals can be computed efficiently and to controllable accuracy. Traditionally, these integrals are tabulated a priori and when performing the integrations for the computation of the impedance matrix are computed using interpolation. A similar scheme is proposed here. However, since the Nyström method is a higher-order scheme, the Sommerfeld integrals must be evaluated to controllable accuracy. Secondly, the precomputation of the Sommerfeld integrals at discrete points must also be performed efficiently and to controllable precision. This is addressed in the following sections. Initially, an efficient means of computing the Sommerfeld integrals is presented in Section 6.2. To this end, an appropriate contour path is introduced that avoids the highly oscillatory behavior of the integrand near branch point singularities and poles. In Section 6.3, an efficient and accurate interpolation method based on a rational function interpolation is introduced. The advantage of this method is that the order of interpolation can be modified to control the accuracy of the interpolation. Furthermore, the method reduces the number of overall points that need to be computed.

6.2 Efficient Computation of the Sommerfeld Integral

The generalized Sommerfeld integral is given by the expression

$$S_n(f)=\int_0^\infty J_n(k_\rho \rho)k_\rho^{\,n+1} f e^{-u_1 z} dk_\rho \tag{6.2}$$

where *f* is a function dependent on the characteristics of the layered media which is assumed to be singular in the region of integration and

$$k_\rho=\sqrt{k^2-k_z^{\,2}} \tag{6.3}$$

$$\rho=\sqrt{x^2+y^2} \tag{6.4}$$

As an example, consider a single-layer planar dielectric substrate with relative permittivity ε_r and thickness *h* backed by a ground plane. The horizontal projection of the magnetic vector potential G_A at the dielectric-air interface ($z = 0$) and due to a source at this interface is expressed as:

$$G_A(\rho)=\int_0^\infty J_0(k_\rho \rho)\frac{1}{D_{TE}}k_\rho dk_\rho \tag{6.5}$$

while the electric scalar potential G_q is expressed as:

$$G_q(\rho)=\int_0^\infty J_0(k_\rho \rho)\frac{N}{D_{TE}D_{TM}}k_\rho dk_\rho \tag{6.6}$$

where

$$N=u_1+u_2\tanh(u_2 h) \tag{6.7}$$

$$D_{TE}=u_1+u_2\coth(u_2 h) \tag{6.8}$$

$$D_{TM}=\varepsilon_r u_1+u_2\tanh(u_2 h) \tag{6.9}$$

$$u_1=jk_{z1}=\left(k_\rho^2-k_1^2\right)^{1/2} \tag{6.10}$$

$$u_2=jk_{z2}=\left(k_\rho^2-k_2^2\right)^{1/2} \tag{6.11}$$

where k_2 is the wave number of the dielectric substrate, and k_1 is the free-space wave number. The integrals in (6.4) and (6.5) are performed on the real axis of the complex k_p plane.

However, the path must be either deformed about the branch point at k_1 and the poles between k_1 and k_2 on the real axis, or a principal value need be evaluated at these points. It can be readily shown that D_{TE} will not have any zeros unless

$$f > \frac{c_0}{4h\sqrt{\varepsilon_r - 1}} \tag{6.12}$$

which corresponds to a relatively thick substrate. On the other hand, D_{TM} will always have at least one pole on the interval of $[k_1, k_2]$. As the frequency is increased, additional poles will be introduced on this interval.

When evaluating (6.5) or (6.6), a principal value integral must be introduced to evaluate the integral at any singularitie lying on the real axis. To this end, the zeroes of D_{TM} and D_{TE} must be found to determine the poles of (6.5) and (6.6). Subsequently, the residues at each pole are then computed. Then, the principle value integral can be. It is noted that for general layered media, the poles must be determined numerically. However, the accuracy of the Sommerfeld integration depends upon the ability to accurately compute the zeroes and residues. Thus, to evaluate the Sommerfeld to high precision, the zeros of D_{TM} and D_{TE} need also be determined to high precision. This is often computationally intensive. Furthermore, near the poles, the integrand becomes highly oscillatory. As a result, computing the Sommerfeld integral to high-precision using an adaptive quadrature scheme is also extremely expensive.

An alternate approach to computing the Sommerfeld integration is to deform the path of integration off the real axis. While an infinite number of paths can be chosen, an effective contour consisting of a semi-elliptic path has been suggested by Gay-Balmaz and Mosig [13]. The semi-elliptic path suggested extends from the origin to a point on the real axis well beyond the zeroes, as shown in Fig. 6.1. The center of the ellipse is chosen at

$$k_c = \frac{k_1\left(1 + \sqrt{\varepsilon_r}\right)}{2} \tag{6.13}$$

so that the path of integration returns to the real axis well beyond any pole.

By deforming the path in this manner, the singularities are avoided and thus the accuracy of the Sommerfeld integration is no longer bound to the accuracy of the prediction of the poles and residues. Secondly, by properly determining the minor axis of the ellipse, the highly oscillatory nature of the integrand is avoided. This greatly improves the efficiency of the computation. It is noted, though, that it is not required to use an elliptic path. In fact, a path through the saddle point would be ideal. However, the elliptic path has the advantage of simplicity and flexibility. Further, the semi-elliptic path is easily parameterized and an adaptive quadrature routine can be used to perform the numerical integration.

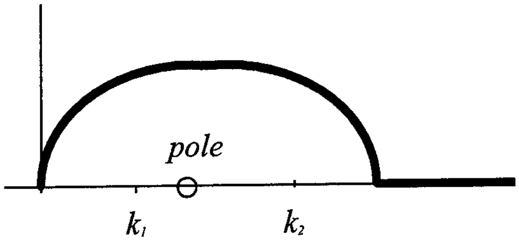

Fig. 6.2 Elliptic path for integrating around poles.

Finally, the integrals in (6.5) and (6.6) are being performed by integrating along the semi-elliptical path along the interval $[0,2k_c]$. This is done using a simple adaptive quadrature scheme. Then, the method of averages [12] is used to perform the integral along the real axis over the interval $[2k_c,\infty]$. This renders an efficient evaluation of the Sommerfeld integrals that can be performed to controllable precision.

As an example, consider a single layer dielectric substrate with relative permittivity of 4.7 backed by a ground plane. The magnetic vector and scalar potentials were computed using (6.5) and (6.6). In order to determine the relative accuracy of the routines, the results were compared to the small argument approximation of the vector and scalar potentials . Initially, the relative percentage of error in the magnitude of the magnetic vector potential as compared to a small argument approximation [14] is illustrated in Fig. 6.2 for substrate thickness of $h = 10^{-3}$ and 10^{-1}. For these computations, the adaptive quadrature requested a relative error of 10^{-3} and used 25 intervals for the method of averages. It is observed that for the thinner substrate the small-argument approximation provides 10^{-5} % accuracy (7 digits) for distances of $10^{-6}\lambda$ or less. For the thicker substrate, the level of accuracy reduces by roughly two orders of magnitude.

Figure 6.3 illustrates the magnitude of the magnetic vector potential versus radial distance over the range of $10^{-8} < \rho < 1$ for substrate thickness of $h = 10^{-3}$ and 10^{-1} as computed from (6.5). To demonstrate the efficiency of the numerical routine, the total number of function evaluations (i.e., the number of evaluations of the integrand) required to compute each point in Fig. 6.3 is illustrated in Fig. 6.4. This includes the contour path integration and the method of averages. It is seen that as the radial distance decreases, the number of points increases. As seen in Fig. 6.2, for small values of ρ, small argument approximations can be used to accurately evaluate the Sommerfeld integral. Nevertheless, for the error criterion specified, at most 1800 evaluations was required. Thus, the computation of Fig. 6.3 can be done in seconds.

The same example is repeated for the electric scalar potential (6.6). These results are again illustrated in Figs. 6.4 through 6.6, with similar results as the magnetic vector potential.

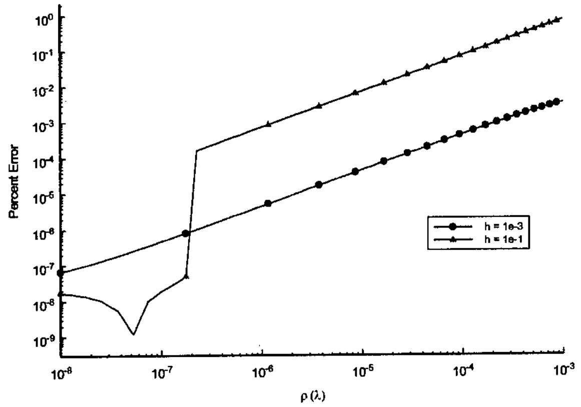

Fig. 6.2. Percent error between magnetic vector potential and a small argument approximation.

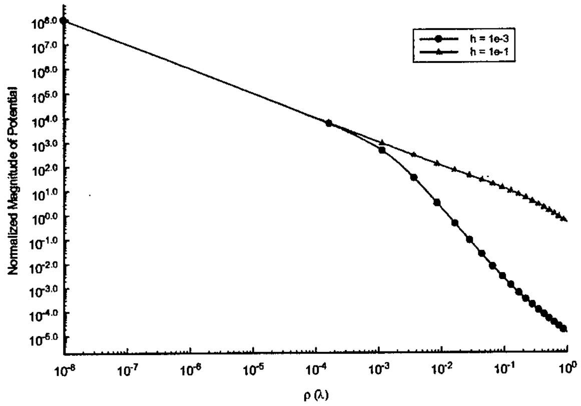

Fig. 6.3 Magnitude of magnetic vector potential.

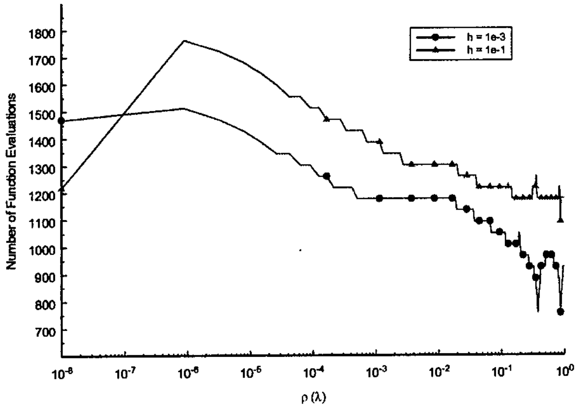

Fig. 6.4 Number of function evaluations for computing potentials in Fig. 6.3.

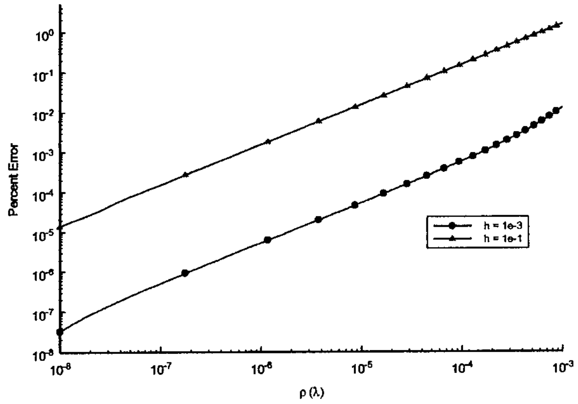

Fig. 6.5 Percent error between electric scalar potential and the small argument approximation.

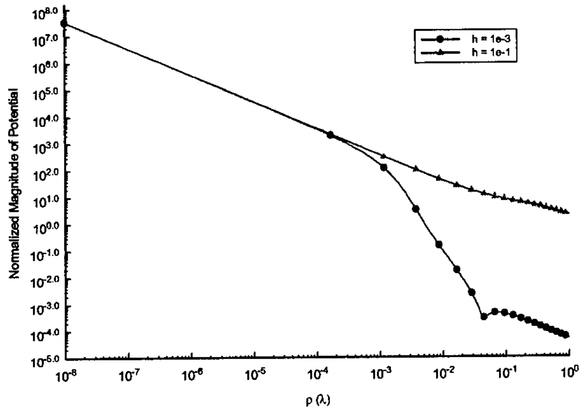

Fig. 6.6 Magnitude of magnetic vector potential.

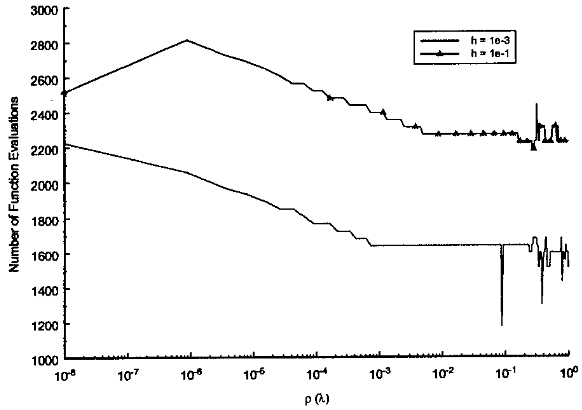

Fig. 6.7 Number of function evaluations for computing potentials in Fig. 6.6.

6.3 Interpolation of the Green's function

Since the proposed numerical scheme is a high-order solution of the MPIE, the Green's function must be evaluated to a controllable accuracy. In the previous section, a means to perform the Sommerfeld integrals to controllable accuracy was presented. Unfortunately, it would be computationally prohibitive to perform the Sommerfeld integration for each value of ρ required by adaptive quadrature evaluation for the impedance matrix. Rather, it is much more efficient to precompute the magnetic vector and scalar potential at discrete points *a priori* and then compute the Green's function for arbitrary values of ρ via an interpolation scheme. It must be realized that to maintain high-order accuracy, the interpolation scheme must be able to interpolate the Green's function as well as its derivative to controllable accuracy. This is the topic of this section.

Due to the azimuthal symmetry of the Green's function, the Sommerfeld integrals can be tabulated as a one-dimensional array if all the conductors are horizontal and are located at the same vertical height. Otherwise, a two-dimensional array need be computed and stored. The discrete distances are sampled based on a logarithmic scaling along the radial direction over a pertinent range to resolve the large scale behavior of the Green's function. The Green's function is thus interpolated based on this logarithmic spacing of points.

It has been found that polynomial interpolation of the Green's function, e.g., Lagrange interpolation polynomials, can not provide controllable accuracy without a very dense sampling of points. This is undesirable since it adds to the precomputation cost, as well as the cost of each interpolation. A more efficient means of interpolation is a rational function interpolation [11]. Specifically, it has been found that a rational function interpolation can estimate the number of data points are necessary to controllable accuracy. Furthermore, efficient schemes of evaluating the rational function interpolation in multiple dimensions have been developed [15].

To this end, we have applied a multidimensional rational polynomial interpolation of the layered Green's function. The interpolation scheme is efficiently applied using the Bulirsch-Stoer algorithm [16], which is a recursive scheme. Again, the data is logarithmically scaled. The Green's function is then computed via interpolation by using local reference points. Specifically, for a given value of ρ, the discrete interpolation points used are determined by a fixed window centered about ρ.

As an example, the magnetic vector potential in Fig. 6.4 with substrate thickness 10^{-3} is interpolated via a rational function interpolation. To this end, the magnetic vector potential was computed at 222 logarithmically spaced points over the range of $\rho \in \left[10^{-7},1\right]\lambda$. Subsequently, the magnetic vector potential was then computed at logarithmically spaced points over this same range not coincident with the original data points. The magnetic vector potential was then predicted using both rational function interpolation and using the Sommerfeld integration. The relative error of the interpolated values versus the integration is illustrated in Figs. 6.8 and 6.9 for the real and the imaginary parts of the vector potential, respectively. The interpolations were done using both a 5 point and a 10 point window. It is observed that for this range of values, the 5 point interpolation provides 2 digits or more of accuracy, and the 10 point window provides at least 6 digits of accuracy relative to the original integral. It is also observed that the error is more accurately predicted for small values of ρ, while larger errors are encountered for larger values of ρ. This is mainly due to the fact that for larger values of ρ the magnetic vector potential is more oscillatory. As a result, denser sampling denser becomes necessary for larger values of ρ.

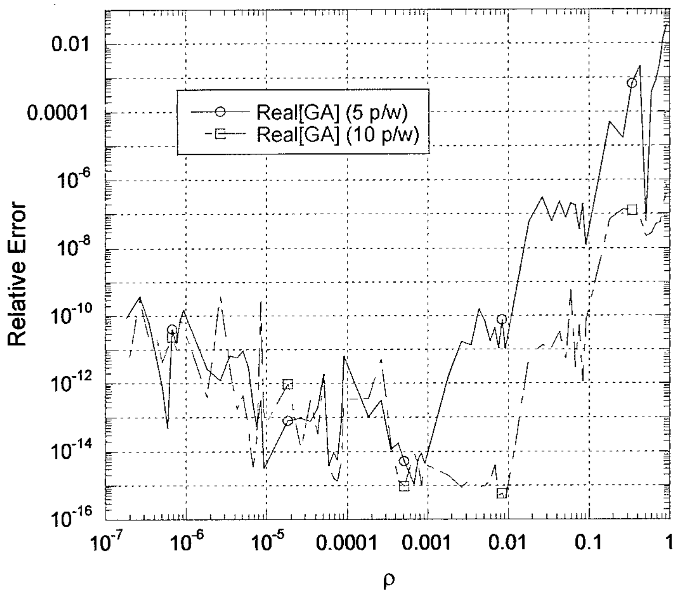

Fig. 6.8 Relative error in the real part of the magnetic vector potential predicted by 5 point and 10 point rational function interpolation over the range of $\left[10^{-7}\lambda, 1\lambda\right]$.

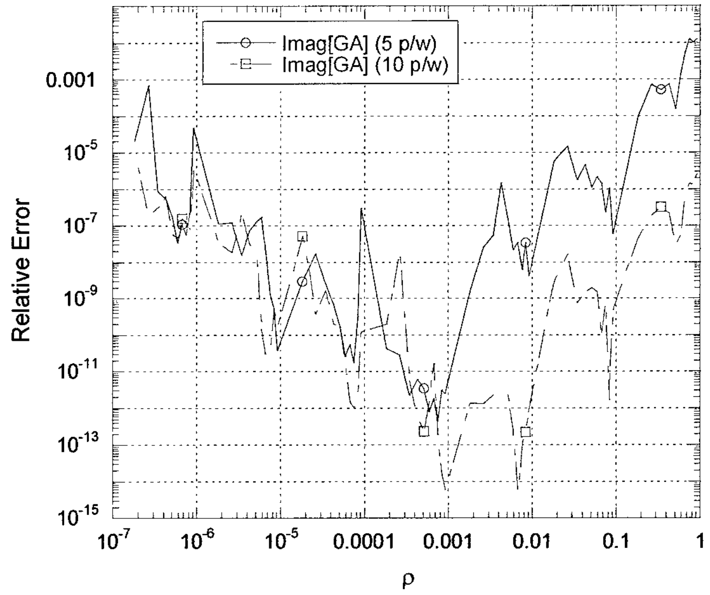

Fig. 6.9 Relative error in the imaginary part of the magnetic vector potential predicted by 5 point and 10 point rational function interpolation over the range of $\left[10^{-7}\lambda, 1\lambda\right]$.

7. Conclusions

In this report, we have summarized the 6 month progress funded under this STIR towards a high-order fast solution of the MPIE for the analysis of microwave circuits printed in a layered media. To this end, a locally corrected Nyström solution of the electric field integral equation (EFIE) and the magnetic field integral equation (MFIE) for the three-dimensional free-space Green's function has been developed. Through numerical examples, it was demonstrated that the LCN technique is high-order convergent. Specifically, exponential convergence is realized by simply increasing the quadrature order of the underlying Nyström scheme. Furthermore, it was demonstrated that high-order convergence is realizable with only modest increases in computational time. It was also demonstrated that high-order convergence can be realized for metallic structures with sharp edges. This was achieved through the use of a Gauss-Jacobi quadrature rule. For flat edges, a Gauss-Jacobi quadrature rule exactly integrates the edge singularity and will provide exponential convergence. For curved edges, the singularity is not represented exactly. However, it is closely approximated, and the LCN method will provide rapid convergence to engineering accuracy.

The advantages of a high-order scheme such as the locally-corrected Nyström scheme is that solutions to engineering accuracy (1 %) can be realized with less resources than a traditional low-order method. More importantly, the LCN method can also offer an error estimate of the final solution with little additional computational overhead.

The second important thrust area presented is in the efficient computation of the layered Green's function. To this end, a contour path originally suggested by Gay-Balmaz and Mosig [13] is utilized along with the method averages [12, 14] to efficiently compute the Sommerfeld integrals to controllable precision. It was then shown that a rational function interpolation of the data then provides a highly efficient means of interpolating the data to controllable accuracy in one and two dimensions.

REFERENCES

[1] S. M. Rao, D. R. Wilton, and A. W. Glisson, "Electromagnetic Scattering by Surfaces of Arbitrary Shape," *IEEE Transactions on Antennas and Propagation*, vol. AP-30, n. May, pp. 409-418, 1982.

[2] L. F. Canino, J. J. Ottusch, M. A. Stalzer, J. L. Visher, and S. M. Wandzura, "Numerical solution of the Helmholtz equation in 2D and 3D using a high-order Nyström discretization," *Journal of Computational Physics*, vol. 146, n. 2, pp. 627-663, 1998.

[3] S. D. Gedney, J. J. Ottusch, P. Petre, J. L. Visher, and S. M. Wandzura, "Efficient high-order discretization schemes for integral equation methods," presented at IEEE International Symposium on Antennas and Propagation, Montreal, Canada, 1997.

[4] R. D. Graglia, D. R. Wilton, and A. F. Peterson, "Higher order interpolatory vector bases for computational electromagnetics," *IEEE Transactions on Antennas and Propagation*, vol. 45, n. March, pp. 329-342, 1997.

[5] L. R. Hamilton, J. J. Ottusch, M. A. Stalzer, R. S. Turley, J. L. Visher, and S. M. Wandzura, "Numerical solution of 2-D scattering problems using high-order methods," *IEEE Transactions on Antennas and Propagation*, vol. 47, n. 4, pp. 683-691, 1999.

[6] J. Strain, "Locally Corrected Multidimensional Quadrature-Rules for Singular Functions," *Siam Journal on Scientific Computing*, vol. 16, n. 4, pp. 992-1017, 1995.

[7] J. A. Stratton, *Electromagnetic Theory*. New York: McGraw-Hill, 1941.

[8] M. G. Duffy, "Quadrature over a pyramid or cube of integrands with a singularity at a vertex," *SIAM Journal on Numerical Analysis*, vol. 19, n. December, pp. 1260-1262, 1982.

[9] S. D. Gedney, "High-order Nyström solution of the EFIE in 3D for structures with edge singularities," presented at IEEE Symposium on Antennas and Propagation/URSI Meeting, Orlando, FL, 1999.

[10] S. D. Gedney, "Application of the High-Order Nyström Scheme to the Integral Equation Solution of Electromagnetic Interaction Problems," presented at IEEE International Symposium on Electromagnetic Compatibility, Washington, D.C., 2000.

[11] W. H. Press, B. P. Flannery, S. A. Teukolsky, and W. T. Vetterling, *Numerical Recipe's: The Art of Scientific Computing*, 2nd ed. New York: Cambridge University Press, 1992.

[12] J. R. Mosig, "Integral Equation Techniques," in *Numerical Techniques for Microwave and Millimeter-Wave Passive Structures*, T. Itoh, Ed. New York: John Wiley & Sons, 1989, pp. 133-213.

[13] P. Gay-Balmaz and J. R. Mosig, "Three-dimensional planar radiating structures in stratified media," *International Journal on Microwave and Millimeter-Wave Computer Aided Engineering*, vol. 7, n. September, pp. 330-343, 1997.

[14] J. R. Mosig and F. E. Gardiol, "A Dynamical Radiation Model for Microstrip Structures," in *Adv. Electron. Electron Phys.*, vol. 59, P. W. Hawkes, Ed. New York: Academic, 1982, pp. 139-237.

[15] W.-H. Tang, "Efficient Microwave Circuit Design Using Full-Wave Analysis, Automated Optimizations, and Multi-dimensional Cauchy Interpolation," M.S. Thesis, Department of Electrical Engineering: University of Kentucky, Lexington, KY, 2000.

[16] J. Stoer and R. Bulirsch, *Introduction to Numerical Analysis*. New York: Springer-Verlag, 1980.